Spatial and temporal variations of Venus haze properties obtained from Pioneer Venus Orbiter polarimetry

C. J. Braak, J. F. de Haan,[1] and J. W. Hovenier[2]

Department of Physics and Astronomy, Free University, Amsterdam, Netherlands

L. D. Travis

NASA Goddard Institute for Space Studies, New York, New York, USA

[1] The spatial and temporal variations of the polarization of light scattered by Venus, as observed by the Pioneer Venus Orbiter between 1978 and 1990, is analyzed in terms of spatial and temporal variations of Venus upper haze properties. Special attention is given to choosing maps with sufficiently accurate geometrical information. This selection involves multiple-scattering calculations for a number of reasonable models for the Venus atmosphere. For a set of observations in four wavelength bands of the Venus disk as a whole or a particular region thereof, observed values of Stokes parameters I and Q were used to obtain the average observed relative Stokes parameter q^{obs}. Subsequently, the haze particle column density and the cloud top pressure were iteratively adjusted until values of q^{obs} at two wavelengths were reproduced. For the planet as a whole, it was found that the haze particle column density decreased gradually during the Pioneer Venus Orbiter mission, whereas little significant temporal variability was found for the cloud top pressure. Similar long-term behavior was derived for selected regions of Venus. Regions at higher latitudes exhibited higher values of both the haze particle column density and the cloud top pressure than regions at lower latitudes. Something similar holds for regions with low solar elevations as compared to regions in which the Sun was close to the zenith. *INDEX TERMS:* 6295 Planetology: Solar System Objects: Venus; 5464 Planetology: Solid Surface Planets: Remote sensing; 5405 Planetology: Solid Surface Planets: Atmospheres–composition and chemistry; *KEYWORDS:* Venus, polarization, haze, clouds, Pioneer Venus Orbiter

1. Introduction

[2] *Hansen and Hovenier* [1974] derived with unprecedented accuracy the refractive index of the Venus cloud particles at wavelengths ranging from 365 to 990 nm from ground-based polarization observations and concluded that the composition of the cloud particles was probably a concentrated sulfuric acid solution. Studies of the infrared spectrum of Venus based on airborne observations [*Pollack et al.*, 1974, 1975, 1978] and data of the Venera 15 orbiter [see, e.g., *Esposito et al.*, 1997] substantiated this conclusion.

[3] *Hansen and Hovenier* [1974] also established the particles to be spherical with a rather narrow size distribution having an effective radius of 1.05 μm and an effective variance of 0.07. They used disk-integrated observations that covered a period of over 40 years. In order to explain measurements obtained by the Pioneer Venus Orbiter Cloud Photopolarimeter (OCPP) between December 1978 and August 1979, *Travis et al.* [1979] and *Kawabata et al.* [1980] required an additional species of particles within and above the clouds. For these particles, *Kawabata et al.* [1980] established an effective radius of 0.25 μm and refractive indices at visible wavelengths approximately equal to those of the cloud particles as

determined by *Hansen and Hovenier* [1974], while the optical thickness of these small particles was significantly larger in both polar regions than near the equator. In situ observations at the cloud tops by the Pioneer Venus Large Probe seemed to be consistent with the presence of two particle size modes [*Knollenberg and Hunten*, 1980; *Donahue and Russell*, 1997]. Ground-based polarimetry in the infrared also showed small particles to be present near the cloud tops [see *Sato et al.*, 1980; *Mukai and Mukai*, 1981]. Also, 4.5- to 5-day periodic fluctuations in the degree of polarization at 3.6 and 3.8 μm were found [*Nagata et al.*, 1984], indicating variability of the optical thickness of the small particles on such timescales.

[4] The OCPP conducted polarization measurements until December 1990. The entire OCPP data set was studied by *Sato et al.* [1996] and *Knibbe et al.* [1998] for the polar regions and the planet as a whole, respectively. They used atmospheric models in which the small particles are confined to a so-called haze layer above the main cloud deck in which only larger particles (with an effective radius of 1.05 μm) reside. *Knibbe et al.* [1997] reported that such a model could explain the OCPP observations equally well as a model in which the small and large particles are mixed within one layer. Both *Sato et al.* [1996] and *Knibbe et al.* [1998] found that the haze optical thickness exhibits a long-term declining trend, upon which variations on smaller timescales are superposed. *Knibbe et al.* [1998] found (1) that for the largest part of the Pioneer Venus Orbiter mission, the cloud top pressure was 10–25 mbar, more or less in agreement with earlier findings, and (2) that at a particular time in 1983, the cloud top seemed to have sunk deep into the atmosphere, while the haze had vanished. *Sato et al.* [1996] also established more accurate values for the refractive index of the haze particles.
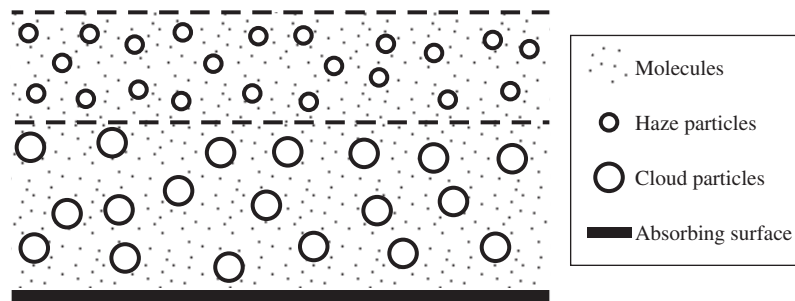

Figure 1. Schematic representation of the atmospheric model used in the analysis.

[5] In this paper we provide a more complete picture of the evolution of the Venus haze by extending the analyses of *Knibbe et al.* [1998] in three ways. First, since we found that some of the OCPP polarimetry data contained inaccurate geometrical information, we performed a strict selection of the most reliable data and reevaluated the findings of *Knibbe et al.* [1998] for the Venus disk as a whole. Second, we divided the planet in nine latitude bands and studied those separately, thus extending the analyses of *Sato et al.* [1996] to midlatitudes and equatorial regions. And third, we investigated whether there is a relationship between haze properties and solar elevation.

2. Pioneer Venus OCPP Observations

[6] The Pioneer Venus Orbiter was launched in May 1978 and inserted into a highly elliptical (periapsis near 200 km altitude, apoapsis near 67,000 km) and nearly polar (inclination about 105°) orbit around Venus in December 1978. The orbital period was ~24 hours. One of the instruments on board the Pioneer Venus Orbiter was the Orbiter Cloud Photopolarimeter (OCPP). This instrument employed three modes of operation: photopolarimetry, imaging, and limb-scan. This paper discusses photopolarimetry only. In 1992, operations of the Pioneer Venus Orbiter were halted. Information on the Pioneer Venus Orbiter and the OCPP is given by *Colin* [1980] and *Russell et al.* [1977], respectively.

[7] Although the data set we consider has been described earlier, for example, by *Kawabata et al.* [1980] and *Knibbe et al.* [1998], we will provide some information on the measurements and also introduce new concepts and specifications which are necessary for selecting polarimetry data with reliable geometrical information (as is further described in section 4 and Appendix A).

[8] With the Pioneer Venus Orbiter rotating with a period of ~12 s, the OCPP employed a spin-scan technique to make a complete observation of the Venus disk. Incoming light passed through a filter wheel, with (among others) three different half-wave retarder positions for each of four wavelength bands centered at 935, 550, 365, and 270 nm. The full widths at half maximum of these bands were 16, 12.5, 25, and 29 nm, respectively. Subsequently, the light from a particular area of the Venus disk was split into two orthogonally polarized beams, whose radiances were measured every 9.52 ms. In between each spacecraft roll, the filter wheel was rotated to the next position. From measurements of three overlapping areas obtained during three successive rolls for a particular wavelength, the brightness I (identical to the Stokes parameter I), the degree of linear polarization P, and the direction of the polarization χ were determined. Here the reasonable assumption that corresponding areas for each of the three rolls overlap completely was made, which is sufficiently accurate for our purposes. The construct of such a triplet of areas is referred to as a pixel and has dimensions on the planet of ~500 km at the subspacecraft point.

[9] P and χ are related to the Stokes parameters I, Q, and U by

$$P = \frac{\sqrt{Q^2 + U^2}}{I} \qquad (1)$$

$$\tan(2\chi) = \frac{U}{Q}, \qquad (2)$$

where Q, U, and χ are defined with respect to the local scattering plane. Stokes parameter V was not measured but can be assumed to be negligible.

[10] Subsequently, using the spacecraft attitude, the OCPP direction of observation, and the position of the spacecraft in its orbit, each pixel was tagged with a celestial longitude and latitude, referenced to the Earth ecliptic of 1950, as well as with values for $\mu = \cos\theta$, $\mu_0 = -\cos\theta_0$, and $\phi - \phi_0$. Here θ and θ_0 are the zenith angles of the directions from the observed point to the observer and from the Sun to the observed point, respectively, and ϕ and ϕ_0 are the corresponding azimuth angles, measured counterclockwise looking downward. The sequence of pixels constructed from three successive spacecraft rolls as described above is referred to as a scan line. Following *Kawabata et al.* [1980], the combination of all scan lines in all four wavelength bands making up one Venus disk is referred to as an (OCPP) polarimetry map. The OCPP produced 1945 of these maps, which are labeled with numbers in the interval 5–4178.

[11] Absolute measurements of the brightness were not used, because errors in the observed brightness up to 10% occurred and the response of the instrument deteriorated during the mission, with no possibility to correct for this. However, the overall relative behavior of the brightness across the disk came in useful for assessing the geometrical information provided with the polarimetry data (see section 4 and Appendix A). Since the degree of linear polarization for a pixel is a relative quantity, its accuracy may be assumed to remain constant throughout the mission, at $\Delta P_\lambda = 0.002$ for wavelengths $\lambda = 365$, 550, and 935 nm. Because for $\lambda = 270$ nm, errors ΔP_{270} were significantly higher, we excluded polarization measurements made at 270 nm from our analyses.

3. Atmospheric Models

[12] In order to infer information about spatial and temporal variations in the atmosphere of Venus, we compared the measurements described in section 2 with results of radiative transfer calculations for several atmospheric models. Each atmospheric model consists of two homogeneous, plane-parallel layers, bounded below by a completely absorbing surface. The lower and upper layers are called cloud layer and haze layer, respectively, and both contain molecules and spherical particles (see Figure 1). We define a large number of different models, instead of one single nominal model, in order to cover all reasonable models for the

Table 1. Parameters of the Atmospheric Model and Their Symbols, as Well as Nominal and Alternative Values as Used in Models A–J2[a]

Parameter	Symbol	Model A Value	Alternative Values (Models)
Cloud Layer Parameters: Particles			
Effective radius, μm	r_{eff}^c	1.05	0.95 (B1); 1.15 (B2)
Effective variance	v_{eff}^c	0.07	
Real refractive index at 365, 550, 935 nm	n_r^c	1.46, 1.44, 1.43	1.445, 1.425, 1.415 (C1); 1.475, 1.455, 1.445 (C2)
Imaginary refractive index at 365, 550, 935 nm	n_i^c	0, 0, 0	2.9×10^{-4}, 2.3×10^{-5}, 1.3×10^{-4} (D)
Column density, μm^{-2}	N_p^c	4.69	3.87 (E1); 9.00 (E2)
Cloud Layer Parameters: Molecules			
Single-scattering albedo at 365, 550, 935 nm	a_m^c	0.5, 1, 1	0.42, 0.91, 0.26 (F1); 0.64, 1, 1 (F2)
Depolarization factor	δ^c	0.079	
Cloud base-top pressure difference, mbar	$\Pi_{cb} - \Pi_{ct}$	997.7	
Haze Layer Parameters: Particles			
Effective radius, μm	r_{eff}^h	0.25	0.20 (G1); 0.30 (G2)
Effective variance	v_{eff}^h	0.17	
Real refractive index at 365, 550, 935 nm	n_r^h	1.46, 1.44, 1.43	1.445, 1.425, 1.415 (H1); 1.475, 1.455, 1.445 (H2)
Imaginary refractive index at 365, 550, 935 nm	n_i^h	0, 0, 0	
Column density, μm^{-2}	N_p^h	0.60	0 (I1); 2.40 (I2)
Haze Layer Parameters: Molecules			
Single-scattering albedo at 365, 550, 935 nm	a_m^h	1, 1, 1	
Depolarization factor	δ^h	0.079	
Cloud top pressure, mbar	Π_{ct}	20	2 (J1); 200 (J2)

[a] Free parameters are printed in bold type. Parameters are dimensionless unless specified otherwise.

Venus atmosphere. A description of this set of models is a prerequisite for understanding the selection of reliable polarimetry maps and for sensitivity studies (see sections 4 and 6).

[13] Below, all parameters of our atmospheric models are discussed. We define 18 models, designated Models A-J2, each corresponding to a set of appropriate choices for their parameter values (see Table 1). Model A acted as the nominal model, and its parameter values are designated nominal parameter values. Using the method that is set forth in section 5, values of designated free parameters (the haze particle column density and the cloud top pressure) were iteratively adjusted until observed quantities were reproduced to within a certain accuracy, leaving the other parameter values fixed. For Model A, absorption in the atmosphere was

neglected at 550 and 935 nm. At 365 nm, molecular absorption was included in the cloud layer.

[14] Models B1-J2 (so-called alternative models) were conceived for studying the sensitivity of the results presented in section 6 to the fixed parameters and for selecting OCPP polarimetry maps with reliable geometrical information (see section 4 and Appendix A). Each of these alternative models differs from Model A in only one parameter value. Note that since the refractive indices and single-scattering albedos may vary with wavelength, each model actually implies three different model realizations, one for each wavelength.

[15] In order to obtain the alternative parameter values for Models D, E1, E2, F1, and F2, multiple-scattering calculations
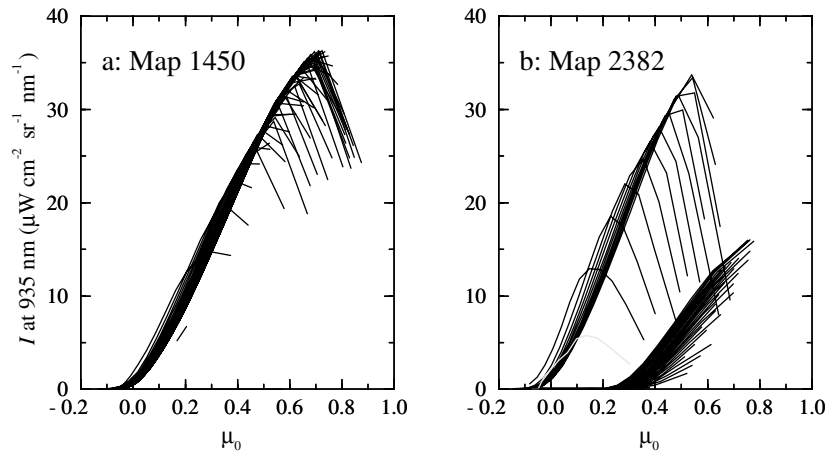

Figure 2. Observed brightness at 935 nm as a function of μ_0 for OCPP polarimetry maps 1450 (26 May 1981, disk center phase angle 111.5°) and 2382 (17 August 1983, 116.7°). Results for pixels from the same scan line are connected by straight lines.
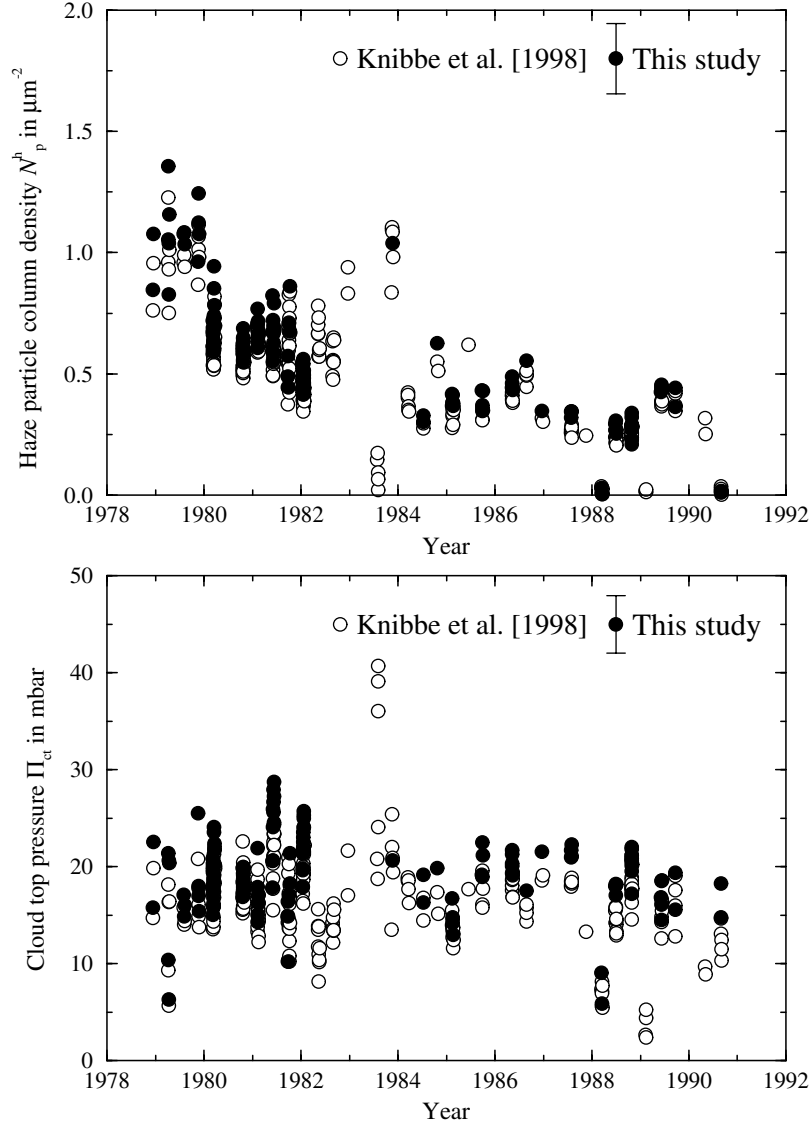
Figure 3. Values of the derived (top) haze particle column density N_p^h and (bottom) cloud top pressure Π_{ct} as functions of time for the Venus disk as a whole for wavelength combination BY and polarimetry maps obtained at phase angles between $80°$ and $100°$. Open circles: results of *Knibbe et al.* [1998] (see their Figure 10), using all applicable maps. Solid circles: our results for reliable maps only, using Model A. The error bars in the upper right corners indicate typical errors if the errors of P are completely correlated for different pixels. If these errors are assumed to be completely uncorrelated, the error bars would be smaller than the circles.

were performed in which the values of the pertinent parameters were varied iteratively until the bounds of a certain interval of the Bond albedo at the three wavelengths were obtained. For these intervals, we used (0.43, 0.57), (0.85, 0.99), and (0.83, 0.97) for 365, 550, and 935 nm, respectively. These bounds are based on results for the Bond albedo obtained by *Travis* [1975] adopting an error of 0.07. Bond albedos calculated for the other models are consistent with the aforementioned intervals. Specifically, the Bond albedos calculated for Model A are 0.48, 0.87, and 0.89 for $\lambda = 365$, 550, and 935 nm, respectively.

3.1. Description of Model Parameters

3.1.1. Cloud particle size distribution (r_{eff}^c, v_{eff}^c). [16] In our models the radii of the cloud particles are distributed according to a gamma distribution [e.g., *Hansen and Travis*, 1974]. We assumed a nominal effective radius $r_{eff}^c = 1.05$ µm and a nominal effective variance $v_{eff}^c = 0.07$ [*Hansen and Hovenier*, 1974]. Models

B1 and B2 have $r_{eff}^c = 0.95$ and 1.15 µm, respectively, consistent with the accuracy given by *Hansen and Hovenier* [1974]. The effective variance remains unchanged throughout this paper.

3.1.2. Cloud particle refractive index $n_r^c - i n_i^c$. [17] For the nominal values of the real part of the refractive index at 365 and 550 nm, we used the values $n_r^c = 1.46$ and 1.44, respectively [*Hansen and Hovenier*, 1974]. For 935 nm we obtained the value $n_r^c = 1.43$ from the values that these authors derived for 550 and 990 nm by linear interpolation in a graph of $[(n_r^c)^2 + 2]/[(n_r^c)^2 - 1]$ versus λ^{-2}. For Models C1 and C2 we chose n_r^c to be 0.015 lower and higher, respectively, at all three wavelengths, in accordance with the accuracies given by *Hansen and Hovenier* [1974]. In all models the cloud particles are nonabsorbing at all wavelengths (i.e., the particle single-scattering albedo equals 1 and the imaginary part of the refractive index $n_i^c = 0$), with the exception of Model D, where we employed $n_i^c = 2.9 \times 10^{-4}$, 2.3×10^{-5}, and 1.3×10^{-4} at 365, 550, and 935 nm, respectively.
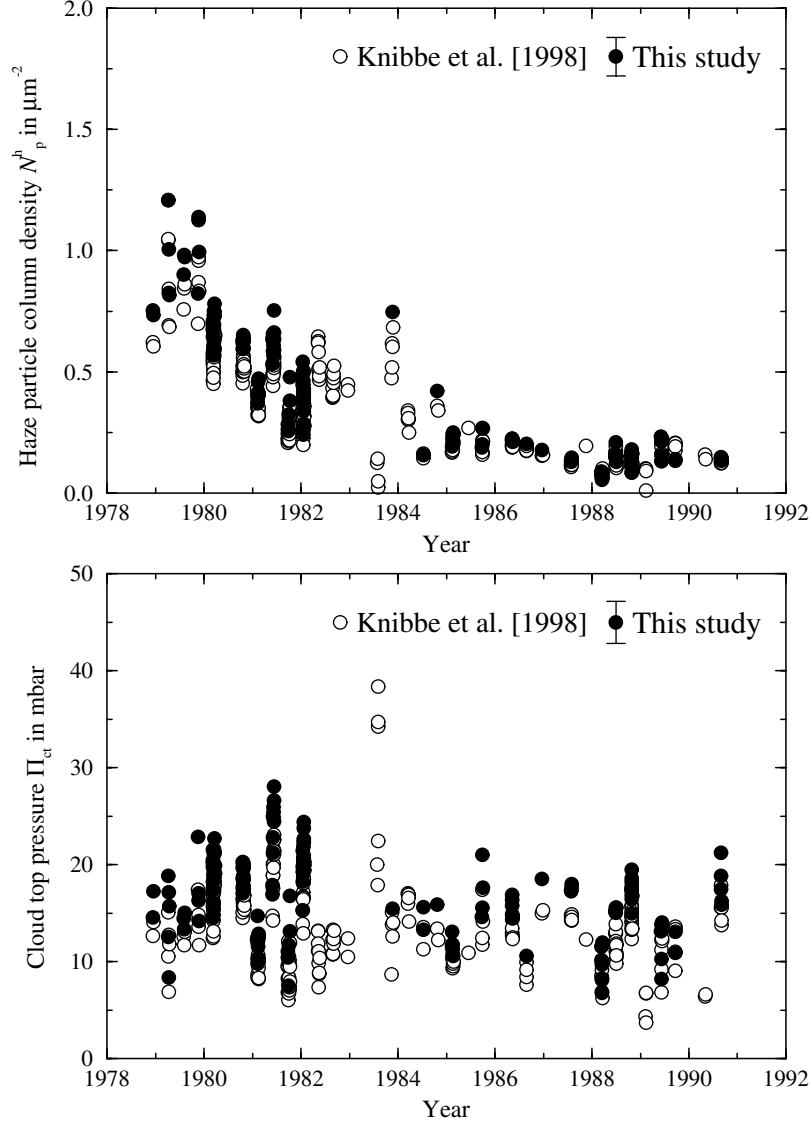
Figure 4. Like Figure 3, but for wavelength combination BR.

The cloud particle absorption corresponding to these values yields the lower bounds of the Bond albedo described above at these wavelengths. Since the nominal values for n_i^c are the minimum values possible, obtaining the upper bounds of the Bond albedo requires varying at least one other parameter, for example, the cloud particle optical thickness or the cloud molecular single-scattering albedo.

3.1.3. Cloud particle column density N_p^c. [18] For this parameter we adopted a nominal value of 4.69 μm^{-2}. Models E1 and E2 have $N_p^c = 3.87$ and 9.00 μm^{-2}, respectively. These values are the lowest and highest values, respectively, that yield Bond albedos within the bounds described above for all three wavelengths. The cloud particle optical thickness $b_p{}^c$ can be calculated from N_p^c using the formula

$$b_p^c = C_{ext}^c \times N_p^c , \qquad (3)$$

where C_{ext}^c is the average extinction cross section of the cloud particles. For the size distribution and refractive indices given above for the nominal model, Mie theory yields $C_{ext}^c = 6.40$, 6.63, and 8.02 μm^2 at 365, 550, 935 nm, respectively. For the nominal value of N_p^c, (3) yields $b_p^c = 30$ at 365 nm, as is consistent with the

range 25–35 deduced from in situ measurements [*Esposito et al.*, 1983; *Ragent et al.*, 1985].

3.1.4. Cloud molecular single-scattering albedo a_m^c. [19] Like *Knibbe et al.* [1998], we adopted the nominal values $a_m^c = 0.5$ at 365 nm and $a_m^c = 1$ at 550 and 935 nm. For Model F1 we employed $a_m^c = 0.42$, 0.91, and 0.26 at 365, 550, and 935 nm, respectively, which yield the lower bounds of the Bond albedo. For Model F2 we used $a_m^c = 0.64$ for 365 nm, which yields the upper bound of the Bond albedo for that wavelength, whereas at 550 and 935 nm we employed the maximum allowable value, that is, the nominal, $a_m^c = 1$. While the latter do not yield the upper bounds of the Bond albedo, the resulting albedos are consistent with the intervals at both wavelengths described above.

3.1.5. Cloud molecular depolarization factor δ^c. [20] We adopted the value $\delta^c = 0.079$, after *Alms et al.* [1975] and *De Haan* [1987]. This value, which is appropriate for the composition of the atmosphere of Venus, is used for all models.

3.1.6. Cloud base–cloud top pressure difference $\Pi_{cb} - \Pi_{ct}$. [21] We employed a value for the cloud molecular optical thickness at 365 nm of $b_{sm}^c = 1.0$, which lies between the values of 0.77 and 1.35 as deduced by *Kawabata et al.* [1980] and *Hansen and Hovenier* [1974], respectively. This value of 1.0 corresponds
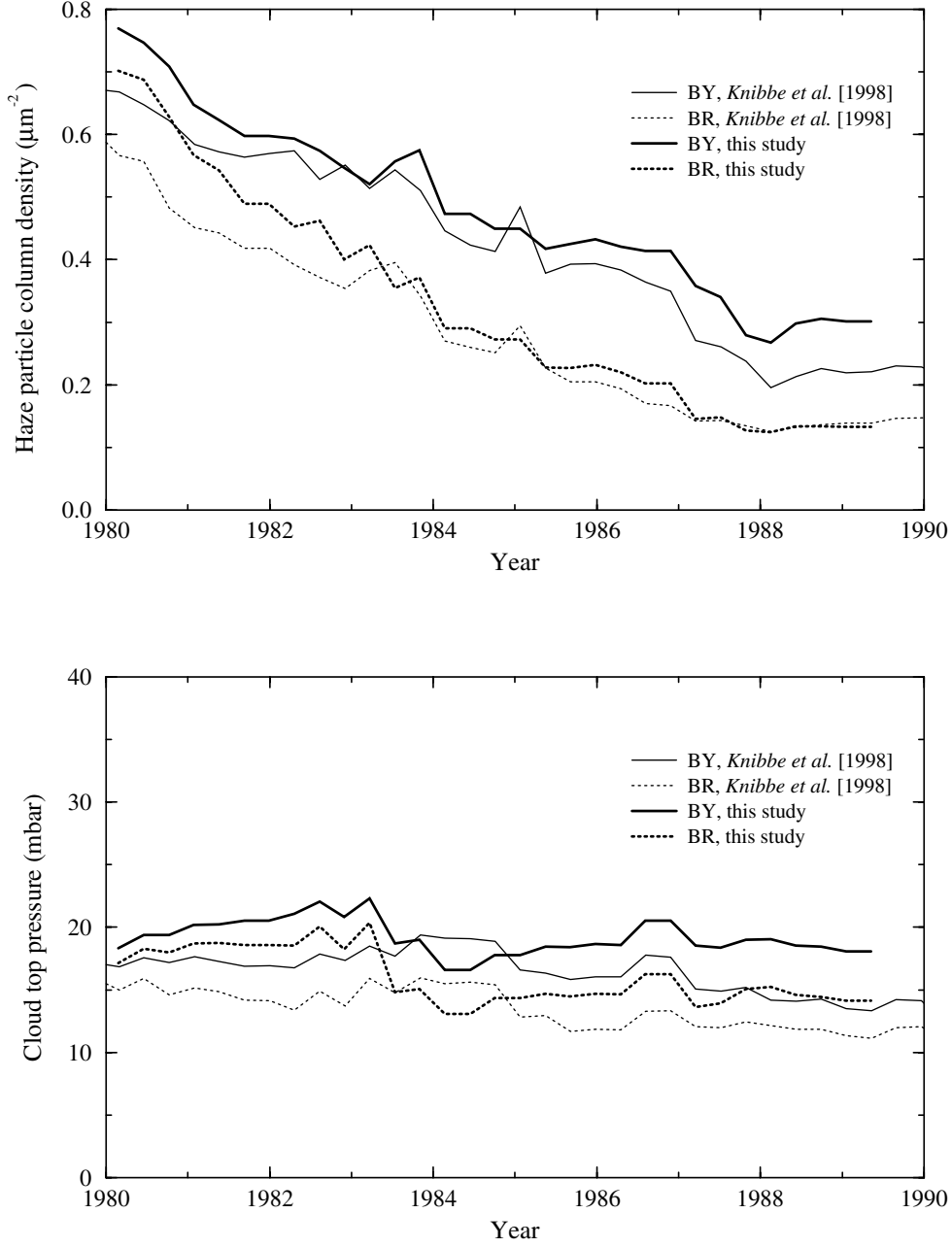
Figure 5. Thick curves: sliding averages corresponding to our results shown in Figures 3 and 4. Averages are computed every 112 days over intervals of 896 days (one half and four Venus siderial years, respectively) and displayed at the midpoints of these intervals. Thin curves: the corresponding sliding averages from *Knibbe et al.* [1998, Figure 13]. Solid curves, wavelength combination BY; dotted curves, wavelength combination BR.

to a pressure difference between the cloud base and cloud top of $\Pi_{cb} - \Pi_{ct} = 997.7$ mbar, using the formula

$$b_{sm} = \frac{1 + 0.013\lambda^{-2}}{6.17 \times 10^4 \lambda^4} \Pi \, , \qquad (4)$$

where b_{sm} is the molecular scattering optical depth at the pressure level Π (in mbar) for the wavelength λ (in μm) [*Hansen and Travis*, 1974]. The value of $\Pi_{cb} - \Pi_{ct}$ remains unchanged throughout this study.

3.1.7. Haze particle size distribution (r_{eff}^h, v_{eff}^h). [22] We employed a gamma distribution for the size distribution of the haze particles with a nominal effective radius $r_{eff}^h = 0.25$ μm [*Kawabata*

et al., 1980]. Models G1 and G2 have $r_{eff}^h = 0.20$ and 0.30 μm, respectively. For the effective variance v_{eff}^h we employed a value of 0.17 [*Kawabata et al.*, 1980] for all models.

3.1.8. Haze particle refractive index $n_r^h - in_i^h$. [23] For the real part of the refractive index of the haze particles, we employed the same nominal values as for the cloud particles, that is, $n_r^h = 1.46$, 1.44, and 1.43, at 365, 550, and 935 nm, respectively. Also, for Models H1 and H2 we used the same values for the haze particles as we did in Models C1 and C2, respectively, for the cloud particles. The nominal and alternative values used here are consistent with refractive indices and their accuracies as derived by *Sato et al.* [1996]. For the imaginary part of the refractive index of the haze particles we used $n_i^h = 0$ (i.e.,

Table 2. Coefficients A and B for Linear Least Squares Fits to the Derived Temporal Variation of the Haze Particle Column Density for the Disk as a Whole, for Both Wavelength Combinations (BY and BR), and Selected Models[a]

Model	A, μm^{-2}		B, μm^{-2} yr^{-1}	
	BY	BR	BY	BR
Model A	0.75 ± 0.02	0.67 ± 0.02	−0.055 ± 0.004	−0.064 ± 0.004
Model C1	0.78 ± 0.02	0.61 ± 0.02	−0.057 ± 0.004	−0.065 ± 0.004
Model D	0.79 ± 0.02	0.72 ± 0.02	−0.058 ± 0.004	−0.059 ± 0.004
Model E2	0.68 ± 0.02	0.63 ± 0.02	−0.059 ± 0.005	−0.068 ± 0.004
Model G1	0.50 ± 0.02	0.65 ± 0.02	−0.035 ± 0.003	−0.062 ± 0.004
Model G2	1.18 ± 0.04	0.71 ± 0.02	−0.093 ± 0.008	−0.069 ± 0.004

[a] See equation (9).

the single-scattering albedo equals 1) at all wavelengths, for all models.

3.1.9. Haze particle column density N_p^h. [24] This is the first free parameter, and values for it are derived using the method described in section 5. However, since the method for selecting maps with accurate geometrical information described in Appendix A requires nominal and alternative values, we introduce here a nominal value of $N_p^h = 0.60$ μm^{-2} and alternative values of $N_p^h = 0$ and 2.40 μm^{-2} (for Models I1 and I2, respectively). The haze particle optical thickness b_p^h is related to N_p^h by a formula similar to (3), with the average extinction cross section of the haze particles, C_{ext}^h, equal to 0.338, 0.252, and 0.100 μm^2 at 365, 550, and 935 nm, respectively, for the nominal model. Then, the nominal and alternative values of N_p^h correspond to haze particle optical thicknesses $b_p^h = 0.20$, 0, and 0.80 at 365 nm, respectively. Values of b_p^h reported so far [*Kawabata et al.*, 1980; *Sato et al.*, 1996; *Knibbe et al.*, 1997] fall within this range.

3.1.10. Haze molecular single-scattering albedo a_m^h. [25] We used $a_m^h = 1$ at all wavelengths, for all models.

3.1.11. Haze molecular depolarization factor δ^h. [26] We used the same value for the haze layer as for the cloud layer, that is, $\delta^h = \delta^c = 0.079$ throughout this investigation.

3.1.12. Cloud top pressure Π_{ct}. [27] Although this is the second free parameter, nominal and alternative values are chosen for the same reason as given above for the haze particle column density. We chose the nominal value $\Pi_{ct} = 20$ mbar. This value corresponds to a haze molecular scattering optical thickness $b_{sm}^h = 0.02$ at 365 nm (see equation (4)). For the alternative values we chose much smaller and much higher values, namely, $\Pi_{ct} = 2$ and 200 mbar for Models J1 and J2, respectively. These values encompass all results reported so far [cf., e.g., *Knibbe et al.*, 1998].

4. Selection of Polarimetry Maps

[28] A selection from the 1945 OCPP polarimetry maps was made on the basis of two criteria. First, as *Knibbe et al.* [1998] showed, the free parameters we selected (the haze particle column density and the cloud top pressure) may be determined most

accurately from observations at phase angles between 80° and 100°. Therefore we made a selection of 270 polarimetry maps with disk center phase angles between those bounds. Second, close inspection of several OCPP polarimetry maps revealed that for some or all scan lines of a number of maps, the geometrical information (μ, μ_0, and $\phi - \phi_0$) is inconsistent with the expected brightness. For example, Figure 2 shows the measured brightness at 935 nm as a function of μ_0, for all scan lines of maps 1450 and 2382. For a plane-parallel atmosphere all such curves are expected to intersect exactly at the origin. For map 1450 this rule seems to hold more or less, although since Venus's atmosphere is curved, some light was detected for $\mu_0 < 0$ owing to twilight effects. However, map 2382 clearly shows two branches (which in itself is reason enough to be suspicious of this map): one with curves that do tend towards the origin and one that has an offset. Note that the shapes of the curves of the latter branch do resemble those of the former. We have concluded that some of the maps in the archived data set have geometries (μ, μ_0, and $\phi - \phi_0$) that are otherwise correct but have been matched with the wrong observations (I, P, and χ) in the scan line owing to incorrect roll position input information and thus have geometries and observations shifted by a number of pixels. We devised a method for estimating the number of pixels that the geometries are shifted with respect to the observations for a scan line. This method involves multiple-scattering calculations for several atmospheric models. Using Model A, we proceeded to select only those maps for which the geometries are shifted by at most one pixel for all scan lines of that map. This was the case for 1257 maps. Next, we repeated the procedure for Models B1-J2, introduced in the preceding section. Thus we made another selection, containing 1234 maps for which the geometries are shifted by at most one pixel with respect to the observations, for all scan lines, using any of our 18 models. Details of this selection method are described in Appendix A. We note that this method may also be important for other data sets obtained by space vehicles.

[29] For the analyses described below, we used the 147 maps out of the 270 maps selected according to their phase angle which are also among the 1234 maps identified as having the most reliable geometrical information. While the latter criterion may

Table 3. Like Table 2, but for Coefficients C and D for Linear Least Squares Fits to the Derived Temporal Variation of the Cloud Top Pressure[a]

Model	C, mbar		D, mbar yr^{-1}	
	BY	BR	BY	BR
Model A	19.6 ± 0.5	18.2 ± 0.5	−0.10 ± 0.10	−0.37 ± 0.10
Model C1	19.1 ± 0.5	16.3 ± 0.5	−0.20 ± 0.09	−0.45 ± 0.10
Model D	19.6 ± 0.5	18.4 ± 0.5	−0.35 ± 0.09	−0.38 ± 0.09
Model E2	28.9 ± 0.6	28.2 ± 0.6	0.43 ± 0.12	0.25 ± 0.12
Model G1	11.6 ± 0.5	12.7 ± 0.5	0.44 ± 0.09	0.17 ± 0.09
Model G2	32.5 ± 0.7	22.2 ± 0.6	−1.12 ± 0.14	−0.75 ± 0.10

[a] See equation (10).

be very strict, we could afford it since enough polarimetry maps remained for performing our analyses.

5. Method of Analysis

[30] For a group of N pixels we define the average relative Stokes parameter q_λ at a particular wavelength λ as follows:

$$q_\lambda = \frac{\sum_{i=1}^{N} Q_{\lambda,i}}{\sum_{i=1}^{N} I_{\lambda,i}}, \qquad (5)$$

where i numbers the pixels of the group under consideration and Q_λ is the second Stokes parameter, expressed in terms of I_λ, P_λ, and χ_λ as

$$Q_\lambda = I_\lambda P_\lambda \cos(2\chi_\lambda). \qquad (6)$$

This follows from (1) and (2) using the rule that Q_λ must have the same sign as $\cos 2\chi_\lambda$ [*Hovenier and Van der Mee*, 1983]. Rather than using "365," "550," and "935" for λ, we will use subscripts "B," "Y," and "R," respectively, representing the color names blue, yellow, and red. We did not use Stokes parameter U in our analyses since its values are generally small compared to Q by virtue of the fact that the scattering plane is used as the reference plane for the determination of Q and U.

[31] Since the error $\Delta(Q_{\lambda,i}/I_{\lambda,i})$ for a pixel i is approximately equal to the error ΔP_λ, that is, 0.002 for all three wavelengths (see section 2), the error Δq_λ^{obs} for a group of pixels is approximately equal to $0.002/\sqrt{N}$, assuming that errors for individual pixels are independent.

[32] We used the following method for estimating values for the free parameters N_p^h and Π_{ct} for a group of pixels. Starting with observations at 365 and 550 nm, we solved the set of equations

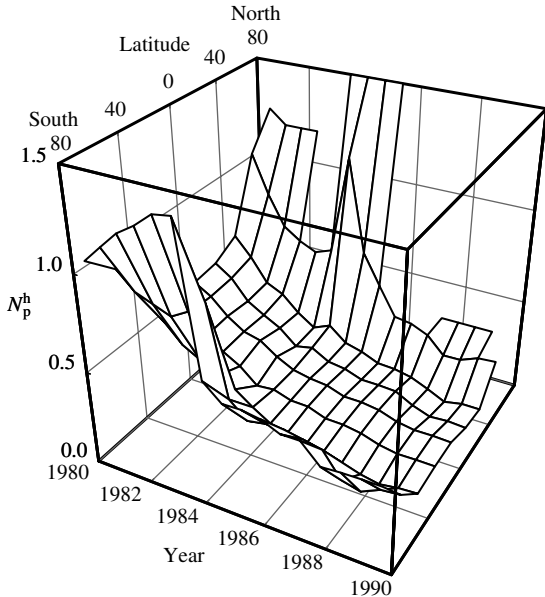$$q_B^{obs} - q_B^{calc}\left(N_p^h, \Pi_{ct}\right) = 0, \qquad (7)$$

Figure 6. Sliding averages of the haze particle column density N_p^h (in μm^{-2}) as a function of time and planetocentric latitude (in degrees). Raw values of N_p^h were calculated from observations integrated over 20°-wide latitudinal bands and subsequently averaged every 224 days over intervals of 896 days. Data points are plotted at the midpoints of intervals. Model A and wavelength combination BR were used for the calculations.
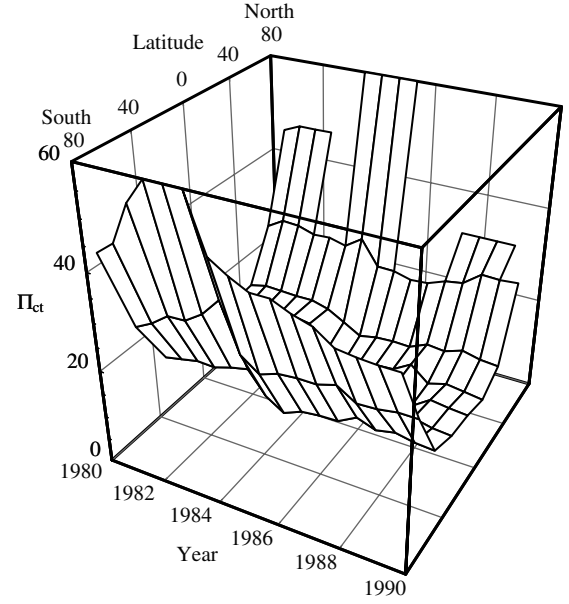

Figure 7. Like Figure 6, but for the cloud top pressure Π_{ct} (in mbar).

$$q_Y^{obs} - q_Y^{calc}\left(N_p^h, \Pi_{ct}\right) = 0, \qquad (8)$$

where the q_λ^{obs} and the q_λ^{calc} were computed using (5) from the observed and calculated values of Q and I for all the pixels in the group, respectively, for their respective wavelengths. Equations (7) and (8) were solved numerically with the iterative Newton-Raphson method [e.g., *Press et al.*, 1992], using fixed differences $\Delta N_p^h = 0.15 \ \mu m^{-2}$ and $\Delta\Pi_{ct} = 0.5$ mbar for calculating the partial derivatives involved. Values of the q_λ^{calc} were computed using the versatile adding/doubling method [*Hansen*, 1971; *Hovenier*, 1971; *De Haan et al.*, 1987]. The iterations were stopped as soon as both left-hand sides were less than 1×10^{-4}.

[33] Errors in the derived parameters were estimated by linearizing and inverting (7) and (8) and then applying the general formula for error propagation by entering either 0.002 or $0.002/\sqrt{N}$ into the resulting formula. The former value must be used if, for different pixels, the errors Δq_B^{obs} and Δq_Y^{obs} are completely correlated; the latter value must be used if these errors are completely uncorrelated.

[34] The discussion above pertains to a biwavelength analysis using observations q_B^{obs} and q_Y^{obs} (wavelength combination "BY"). Wavelength combination "BR" was also used, employing a similar method.

6. Results for the Disk as a Whole

[35] In order to reevaluate the findings of *Knibbe et al.* [1998], who did not consider the reliability of maps, we applied the method described in section 5 to the disk of Venus as a whole. Since the plane-parallel approximation is less accurate for small values of μ and μ_0, the summation in (5) is taken over all pixels of a particular map with both μ and μ_0 greater than 0.2. Consequently, we do not expect that the plane-parallel approximation influences our results [see, e.g., *Van de Hulst*, 1980, section 19.2.2].

[36] We derived values of N_p^h and Π_{ct} for all 147 selected maps using for the fixed parameters Model A, which is essentially identical to the model employed by *Knibbe et al.* [1998]. The solid circles in Figures 3 and 4 show the resulting haze particle column density and cloud top pressure as functions of time, for wavelength combinations BY and BR, respectively. For compar-

Table 4. Coefficients A, B, C, and D for Linear Least Squares Fits to the Derived Temporal Variations of the Haze Particle Column Density and the Cloud Top Pressure for Nine Different Latitude Bands[a]

Latitude, deg	A, μm^{-2}	B, μm^{-2} yr^{-1}	C, mbar	D, mbar yr^{-1}
(−90, −70)	1.27 ± 0.05	−0.092 ± 0.010	51.1 ± 2.0	−0.51 ± 0.40
(−70, −50)	0.96 ± 0.03	−0.085 ± 0.006	27.5 ± 1.0	0.02 ± 0.20
(−50, −30)	0.63 ± 0.02	−0.064 ± 0.004	15.6 ± 0.5	−0.10 ± 0.10
(−30, −10)	0.56 ± 0.02	−0.053 ± 0.004	15.4 ± 0.6	−0.44 ± 0.11
(−10, +10)	0.56 ± 0.02	−0.051 ± 0.004	15.7 ± 0.6	−0.55 ± 0.12
(+10, +30)	0.57 ± 0.02	−0.057 ± 0.004	15.4 ± 0.6	−0.60 ± 0.10
(+30, +50)	0.61 ± 0.03	−0.067 ± 0.005	15.1 ± 0.6	−0.10 ± 0.11
(+50, +70)	0.92 ± 0.05	−0.086 ± 0.008	24.8 ± 1.1	0.23 ± 0.21
(+70, +90)	1.57 ± 0.10	−0.145 ± 0.019	43.2 ± 2.4	−0.21 ± 0.45

[a] See equations (9) and (10). Only Model A and wavelength combination BR were used. Latitudes are planetocentric.

ison, the open circles in these figures show the results of *Knibbe et al.* [1998] (see their Figure 10). There are fewer solid circles than open circles in Figures 3 and 4 owing to our strict selection procedure (outlined in section 4). This is especially noticeable in 1983. Consequently, there is no evidence in our results for the anomaly that is reported by *Knibbe et al.* [1998], namely, that in 1983 the cloud top pressure suddenly rose while the haze particles almost disappeared (see the open circles in Figures 3 and 4).

[37] The values that we derived for the selected maps agree quite well with the values that *Knibbe et al.* [1998] derived for the same maps. Differences are typically not larger than 0.1 μm^{-2} for N_p^h and 2 mbar for Π_{ct}. These small differences are mainly caused by the use of a different stop criterion for the iterations of (7) and (8) and minute round-off errors introduced in converting the parameter values in *Knibbe et al.*'s [1998] nominal model to those in ours, since our models involve a slightly different set of model parameters. As these differences are small, it is not surprising that the general temporal behaviors of the haze particle column density and the cloud top pressure reported by *Knibbe et al.* [1998] are reproduced in our results. That is, (1) both quantities varied irregularly between 1978 and 1990, (2) the haze particle column density shows a gradual decrease during this period, and (3) no significant trend is visible for the cloud top pressure. The latter two points are especially illustrated by the sliding averages of both *Knibbe et al.*'s [1998] and our results (see Figure 5).

[38] For each wavelength combination we fitted linear functions $x(t)$ and $y(t)$,

$$x(t) = A + Bt, \qquad (9)$$

$$y(t) = C + Dt, \qquad (10)$$

to the derived time series of N_p^h and Π_{ct}, respectively. Here t is the time since 1 January 1980, and coefficients A, B, C, and D are calculated by linear least squares fitting over the entire time interval. Results with pertinent errors are shown in Tables 2 and 3. Clearly, for Model A the values of A and C do not depend much on the wavelength combination employed, given the errors listed. However, the values of B and D do depend on the wavelength combination, caused by a discrepancy between the results for different wavelength combinations in the second half of the mission. This is also evident in Figure 5.

[39] In order to investigate the sensitivity of these results to variations of the fixed parameters, we repeated the analysis for all alternative models introduced in section 3. In Tables 2 and 3, results are given only for those alternative models that yielded an extreme value for one or more of the coefficients A−D for at least one wavelength combination. Clearly, for any choice of the fixed parameters and any wavelength combination, the haze particle column density decreased significantly during the Pioneer Venus Orbiter mission. On the other hand, whether the cloud top pressure increased or decreased during this period appears to be model-dependent, but for any model the long-term temporal variation of

the cloud top pressure is much less than that of the haze particle column density. Also, for some models the derived values of the coefficients A, B, C, and D are more consistent between wavelength combinations BY and BR than for other models, which may provide hints for improving the nominal atmospheric model. Lastly, the results for A and C are less model-dependent for wavelength combination BR than for wavelength combination BY, which is consistent with the findings of *Knibbe et al.* [1998].

[40] In all of our analyses we chose $N_p^h = 0.3$ μm^{-2} and $\Pi_{ct} = 1$ mbar as our first guesses. The algorithm turned out to be insensitive to reasonable different first guesses. In a number of cases, no solutions were found for the first guesses we tried. Since almost all of these cases involve maps that were obtained within a few days of maps for which very low haze particle column densities were derived (the algorithm was forced to attempt negative values for one or both parameters), we think that there are in fact no solutions for those maps. With Model A this occurred for eight maps for wavelength combination BY and for none for wavelength combination BR. None of these cases involved maps obtained in 1983, so the disappearance of indications for the anomalous behavior
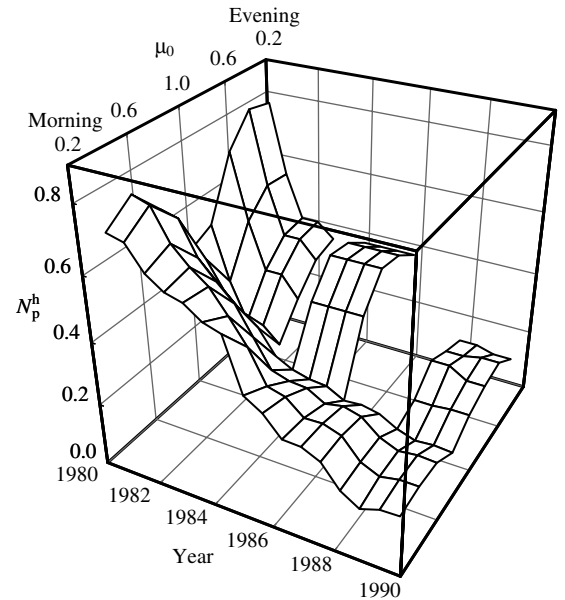

Figure 8. Sliding averages of the haze particle column density N_p^h (in μm^{-2}) as a function of time and μ_0. Raw values of N_p^h were calculated from observations integrated over 0.2-wide μ_0 ranges, distinguishing between maps showing the morning terminator and those showing the evening terminator, and subsequently averaged every 224 days over intervals of 896 days. Data points are plotted at the midpoints of intervals. Model A and wavelength combination BR were used for the calculations.
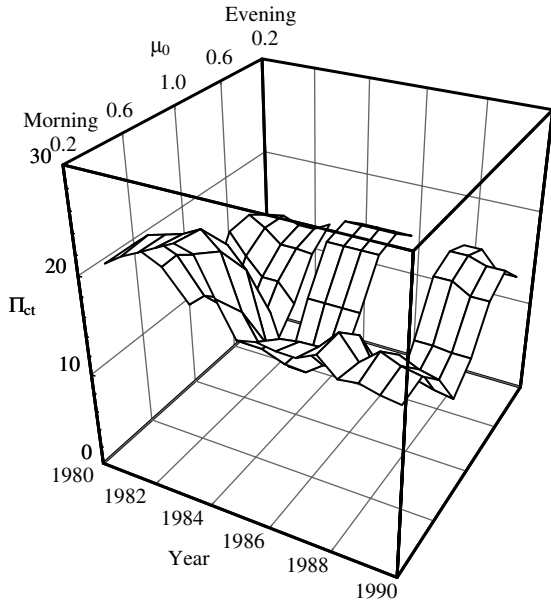
Figure 9. Like Figure 8, but for the cloud top pressure Π_{ct} (in mbar).

referred to above is solely due to our discarding of maps with unreliable geometrical information.

7. Results for Selected Parts of Venus

[41] Having reproduced the decrease in haze optical thickness during the 1980s for Venus as a whole, it is interesting to use a similar approach in order to find out how this decrease evolved for different regions of Venus. For instance, dynamical processes may cause the haze to develop differently in regions near the equator compared to regions near the poles. Or, if the haze is produced photochemically, its density may be coupled to the elevation of the Sun above the horizon. We conducted two studies to investigate those suggestions in more detail. Since for the disk as a whole the results in Tables 2 and 3 turned out to be less model-dependent for wavelength combination BR than for wavelength combination BY, we restricted ourselves in both studies to the former wavelength combination. We used Model A for the values of the fixed parameters. Again, N_p^h and Π_{ct} were employed as free parameters, and pixels were considered only if their values of μ and μ_0 exceeded 0.2.

[42] For the first study we considered nine bands, each 20° wide in planetocentric latitude, for which we repeated the analysis that was described for the disk as a whole in section 7. The method employed was identical, but the summation (see equation (5)) was taken over all pixels for which the planetocentric latitude is within the range corresponding to the respective band. For this purpose, celestial coordinates (see section 2) were converted to IAU planetocentric coordinates. Sliding averages and linear fits of the haze particle column density and the cloud top pressure as functions of time were computed for each latitude band. Figures 6 and 7 show the sliding averages as functions of latitude and time, and Table 4 shows the coefficients of (9) and (10) for each latitude band with the pertinent errors. The raw results (before computing the sliding averages) exhibited, superposed on the long-term trends, large short-term variations for all latitude bands.

[43] Clearly, near the start of the Pioneer Venus Orbiter mission, the haze was more prominent near the poles than near the equator. Also, the behavior of the haze particle column density was remarkably symmetric with respect to the equator. A decreasing trend of the haze column density was found for all latitudes, albeit stronger in more poleward regions. In the regions with latitudes between 70° and 90°, the sliding averages of the haze particle column density appears to have decreased less steadily than in the other bands, possibly owing to poor statistics, since there are fewer maps showing these regions, and those maps showing them have fewer pixels in these regions. This is reflected in the larger errors for the coefficients given in Table 4 for high latitudes. Like the haze particle column density, the cloud top pressure is highest at high latitudes. But unlike the haze particle column density, the cloud top pressure decreased in time for some latitude bands, whereas it increased for others.

[44] For the second study we grouped pixels not according to their planetocentric latitudes, but according to their values of μ_0. Four ranges were defined, and we distinguished between maps showing the morning terminator and those showing the evening terminator. Note that pixels with $\mu_0 \leq 0.2$ were not used. Other than the grouping criterion, we proceeded in the same manner as in the first study. Again, large short-term variations were derived, superposed on long-term trends. Sliding averages of N_p^h and Π_{ct} are shown in Figures 8 and 9, respectively, and coefficients of (9) and (10) are shown in Table 5 with the pertinent errors. It should be noted that there are significantly more maps showing the morning terminator (117) than maps showing the evening terminator (30). This caused the gaps on the evening sides of Figures 8 and 9.

[45] As in the first study, the haze particle column density decreased gradually in time for all pixel groups. For higher solar elevations (large μ_0) the sliding averages of the haze particle column density were smaller in 1980 but decreased more slowly than for lower solar elevations (small μ_0). The behavior of the haze particle column density was remarkably symmetric in the sense that the results for a particular range of μ_0 for maps showing the morning terminator are approximately the same as those for the corresponding range of μ_0 for maps showing the evening termi-

Table 5. Like Table 4, but for Four Different Ranges of μ_0 and Separately for Maps Showing the Morning Terminator and Those Showing the Evening Terminator[a]

μ_0	A, μm^{-2}	B, μm^{-2} yr^{-1}	C, mbar	D, mbar yr^{-1}
		Morning Terminator		
(0.2, 0.4)	0.70 ± 0.02	−0.066 ± 0.004	22.1 ± 0.6	−0.54 ± 0.11
(0.4, 0.6)	0.73 ± 0.02	−0.069 ± 0.004	21.8 ± 0.6	−0.54 ± 0.11
(0.6, 0.8)	0.62 ± 0.02	−0.057 ± 0.003	18.2 ± 0.7	−0.50 ± 0.12
(0.8, 1.0)	0.45 ± 0.02	−0.042 ± 0.003	12.0 ± 0.6	−0.34 ± 0.11
		Evening Terminator		
(0.2, 0.4)	0.76 ± 0.06	−0.083 ± 0.014	14.1 ± 0.8	−0.07 ± 0.18
(0.4, 0.6)	0.77 ± 0.07	−0.078 ± 0.015	15.0 ± 0.9	0.05 ± 0.20
(0.6, 0.8)	0.68 ± 0.06	−0.068 ± 0.014	14.0 ± 1.1	−0.04 ± 0.26
(0.8, 1.0)	0.49 ± 0.05	−0.048 ± 0.012	9.7 ± 1.0	0.04 ± 0.22

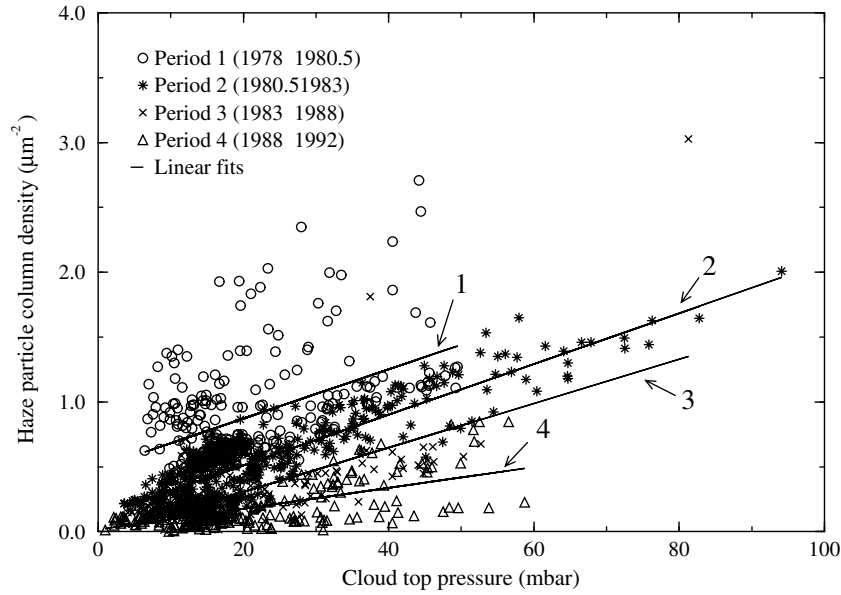[a] Only Model A and wavelength combination BR were used.

Figure 10. N_p^h derived for all nine latitude bands of all selected maps versus the corresponding value of Π_{ct}. The observations are grouped in four periods. The straight lines are least squares fits. Model A and wavelength combination BR were used for the calculations.

nator. The sliding averages of the cloud top pressure in 1980 were significantly higher on the morning hemisphere than on the evening hemisphere, but the morning hemisphere exhibited a cloud top pressure that was slightly decreasing in time for all μ_0 ranges, whereas there was no significant trend for this quantity in the evening hemisphere.

8. Concluding Remarks

[46] Figures 6–9, which show results averaged over time intervals, seem to imply that in regions where the cloud tops were relatively deep in the atmosphere (high Π_{ct}), the haze particles were relatively numerous (high N_p^h). Graphs of N_p^h versus Π_{ct} for individual latitude bands (Figure 10) and solar elevation bands (Figure 11) indeed show a correlation between these quantities. In Figures 10 and 11, four different periods are considered, the boundaries of which correspond to the gaps in the observations near years 1980.5, 1983, and 1988 (see Figures 3 and 4). For the latitude bands the correlation coefficients are 0.48, 0.88, 0.69, and 0.66, for Periods 1, 2, 3, and 4, respectively. For the solar elevation bands these coefficients are 0.24, 0.68, 0.32, and 0.40, respectively. The correlation is strongest in Period 2 (years 1980.5–1983) in Figure 10 as well as in Figure 11. One can speculate on the origin of these correlations. Particles at the top of the cloud may break up into haze particles more easily in some regions than others, so that both the amount of haze particles and the cloud top pressure are relatively large in the former regions. Alternatively, haze particles
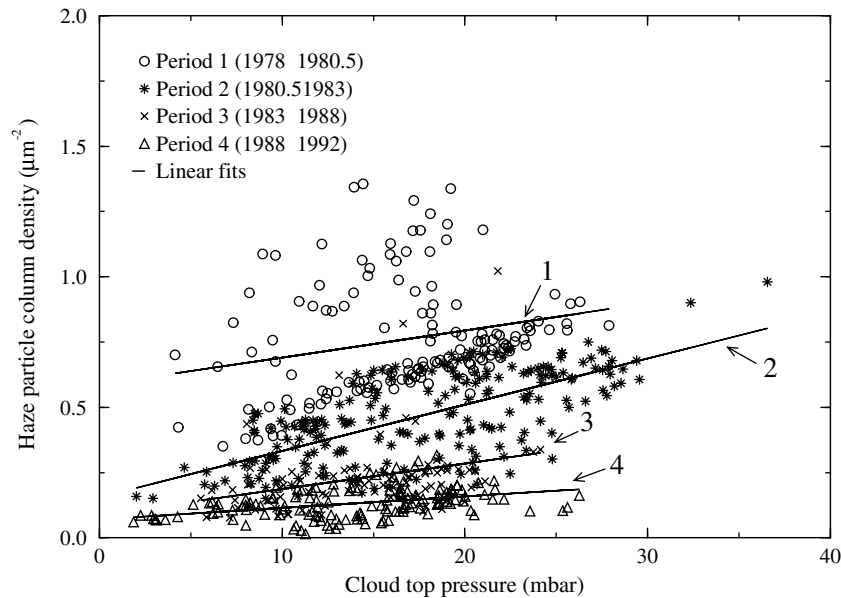

Figure 11. Like Figure 10, but for the eight "solar elevation bands."

Table A1. Data from a Typical Scan Line From the OCPP Polarimetry Data Set[a]

I_R	μ	μ_0	i
15	−2.00	−2.00	1
24	−2.00	−2.00	2
74	0.12	−0.07	3
160	0.24	0.05	4
260	0.31	0.13	5
358	0.36	0.18	6
439	0.40	0.22	$i_1 = 7$
503	0.42	0.25	8
551	0.43	0.27	9
584	0.44	0.29	10
604	0.44	0.30	11
611	0.43	0.30	12
606	0.42	0.29	13
583	0.39	0.28	14
540	0.36	0.26	15
456	0.31	0.22	$i_2 = 16$
333	0.23	0.16	17
199	0.09	0.04	18
75	−2.00	−2.00	19
21	−2.00	−2.00	20
17	−2.00	−2.00	$N_{pix} = 21$

[a] This particular scan line is part of map 1096, which was obtained on 27 December 1980 at a phase angle of 13.9°. Given are the brightness at 935 nm I_R in digital numbers, μ, and μ_0, taken from the data file, and the pixel number i introduced in Appendix A. For pixels off the visible disk of Venus, μ and μ_0, were set to −2.00.

are perhaps transported from other regions if the top of the cloud deck sinks deeper in the atmosphere. Another possibility is that small (haze) particles are in some regions located in between the large (cloud) particles so that a lowering of only the large particles entails an increase of the column density of the small particles above the cloud deck.

[47] Studies of sulfur dioxide (SO_2) at the Venus cloud tops that cover approximately the same period as the results presented here show a gradual decrease of the SO_2 abundance with time [*Esposito et al.*, 1988; *Na et al.*, 1990]. *Esposito et al.* [1988] report a correlation coefficient of 0.8 between the decrease of SO_2 abundance and that of the polar haze optical thickness. The results presented in Figures 6 and 8 suggest that such a correlation may be present for any region on the planet. Therefore our results, together with spatially resolved observations of SO_2, may enhance our

understanding of the chemical connection between the amounts of SO_2 and sulfuric acid in the atmosphere of Venus.

Appendix A: Assessing Geometrical Information of OCPP Polarimetry Maps

[48] In this appendix a method is presented that we used to assess the reliability of the geometrical information that comes with the OCPP polarimetry maps. Application of such a method is necessary, since close inspection of several OCPP polarimetry maps revealed that for some or all scan lines of a number of maps, the geometrical information (μ, μ_0, $\phi - \phi_0$) is incorrect (see section 4). The main assumption in this appendix is that a scan line may in principle be corrected (if necessary) by shifting tabulated values of μ, μ_0, and $\phi - \phi_0$ with respect to tabulated values of I, P, and χ. This assumption follows from the nature of the spin-scan technique for imaging and the fact that the assignment of appropriate geometrical information entails the accurate location of the target body in the scan. Accordingly, the method set forth in this appendix may be expected to be applicable to other data acquired using the spin-scan technique.

[49] For the scattering geometries of any scan line, we performed multiple-scattering calculations for all models introduced in section 3. Because these models are horizontally homogeneous, we focused on the brightness at 935 nm, I_R, since measurements of that quantity exhibit very little horizontal variability. Also, at this wavelength, calculated theoretical brightnesses are relatively insensitive to most of the model parameters.

[50] For the multiple-scattering calculations we used the adding/doubling method. Since this method requires plane-parallel atmospheric models, we only consider geometries with $\mu > 0.2$ and $\mu_0 > 0.2$, consistent with the analyses described in sections 6 and 7. We number the pixels on a scan line consecutively from $i = 1$ to $i = N_{pix}$. Further, the first pixel with μ, $\mu_0 > 0.2$ is numbered i_1, and the first pixel beyond i_1 that does not obey this requirement is numbered $i_2 + 1$, so that pixel number i_2 usually is the last pixel on the scan line obeying μ, $\mu_0 > 0.2$. This numbering is illustrated in Table A1.

[51] Results of calculations are compared with observations as follows. We define for a scan line

$$\chi_n^2(s) = \sum_{i=i_1}^{i_2} \left(\frac{s \cdot I_{R,i}^{calc}}{I_{R,i+n}^{obs}} - 1 \right), \tag{A1}$$
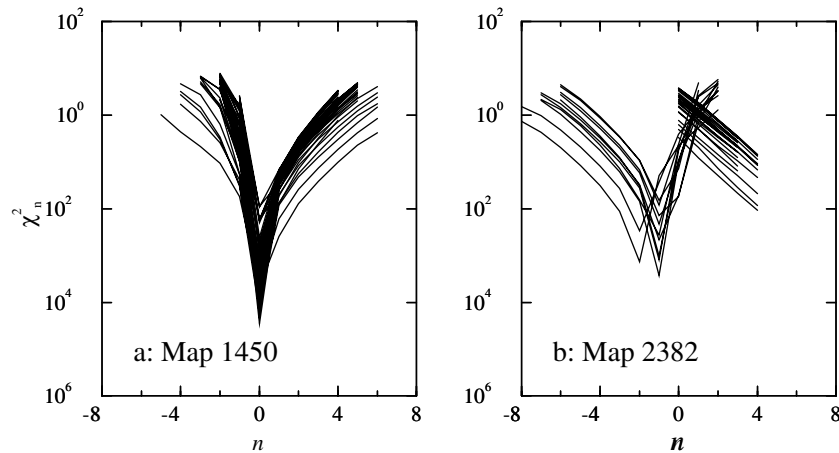

Figure A1. Goodness-of-fit parameter χ_n^2 as a function of n, the number of pixels over which the observations are displaced, for all scan lines of the same OCPP polarimetry maps used in Figure 2. Model A was used for the calculations.

where n is the number of pixels over which the measured values are shifted before being compared with the calculated values, so that $n = 1 - i_1, \ldots, N_{pix} - i_2$. Here $I_{R,i}^{calc}$ and $I_{R,i}^{obs}$ are the calculated and observed values of the brightness at 935 nm, respectively, for the ith pixel of the scan line. Also, a scaling parameter s appears to allow better fits (smaller values of $\chi_n^2(s)$). The rationale behind this is that the responsivity of the detector declined with time, making absolute calibration of the brightness virtually impossible. The minimum of $\chi_n^2(s)$ as a function of s will be referred to as χ_n^2, which may be regarded as a goodness-of-fit parameter. The value of n that minimizes χ_n^2 will be denoted as n_{min}. If, for a particular model, $|n_{min}| \leq 1$ for a scan line, we call that scan line "reliable for that model". If, for a particular model, $|n_{min}| \leq 1$ for all scan lines at 935 nm of a polarimetry map, we call that map "reliable for that model."

[52] First, we followed this procedure for Model A. Figure A1 shows χ_n^2 for this model as a function of n for all 935 nm scan lines of maps 1450 and 2382. Figure A1a shows that all these scan lines of map 1450 have $n_{min} = 0$. Therefore this map is considered to be a reliable map for Model A. For map 2382 (see Figure A1b) the two branches we saw in Figure 2 reappear. It shows that even the branch that looked rather good in fact contains scan lines that have $n_{min} = -2$. Therefore map 2382 is not a reliable map for Model A. After applying the procedure for all 1945 OCPP polarimetry maps, we produced a set of 1257 maps that are reliable for Model A.

[53] In the analyses described in the main text, parameter values are varied in order to explain the measurements. Therefore it is important to know to what extent the composition of the set of reliable maps depends on these parameter values. For this purpose, we repeated the selection procedure for all 17 alternative models introduced in section 3. In this manner, we produced sets of reliable maps, counting between 1240 and 1262 maps. From these sets, 1234 maps turned out to be reliable for all 18 models. Thus our selection criterion does not depend much on the model characteristics.

References

Alms, G. R., A. K. Burnham, and W. H. Flygare, Measurement of the dispersion in polarizability anisotropies, *J. Chem. Phys.*, *63*, 3321–3326, 1975.

Colin, L., The Pioneer Venus program, *J. Geophys. Res.*, *85*, 7575–7598, 1980.

De Haan, J. F., Effects of aerosols on the brightness and polarization of cloudless planetary atmospheres, Ph.D. thesis, Free Univ., Amsterdam, Netherlands, 1987.

De Haan, J. F., P. B. Bosma, and J. W. Hovenier, The adding method for multiple scattering calculations of polarized light, *Astron. Astrophys.*, *183*, 371–391, 1987.

Donahue, T. M., and C. T. Russell, The Venus atmosphere and ionosphere and their interaction with the solar wind: An overview, in *Venus II*, edited by S. W. Bougher, D. M. Hunten, and R. J. Phillips, pp. 3–31, Univ. of Ariz. Press, Tucson, 1997.

Esposito, L. W., R. G. Knollenberg, M. Y. Marov, O. B. Toon, and R. P. Turco, The clouds and hazes of Venus, in *Venus*, edited by D. M. Hunten et al., pp. 484–564, Univ. of Ariz. Press, Tucson, 1983.

Esposito, L. W., M. Copley, R. Eckert, L. Gates, A. I. F. Stewart, and H. Worden, Sulfur dioxide at the Venus cloud tops, 1978–1986, *J. Geophys. Res.*, *93*, 5267–5276, 1988.

Esposito, L. W., J.-L. Bertaux, V. Krasnopolsky, V. I. Moroz, and L. V. Zasova, Chemistry of lower atmosphere and clouds, in *Venus II*, edited by S. W. Bougher, D. M. Hunten, and R. J. Phillips, pp. 415–458, Univ. of Ariz. Press, Tucson, 1997.

Hansen, J. E., Multiple scattering of polarized light in planetary atmospheres, Part I, The doubling method, *J. Atmos. Sci.*, *28*, 120–125, 1971.

Hansen, J. E., and J. W. Hovenier, Interpretation of the polarization of Venus, *J. Atmos. Sci.*, *31*, 1137–1160, 1974.

Hansen, J. E., and L. D. Travis, Light scattering in planetary atmospheres, *Space Sci. Rev.*, *16*, 527–610, 1974.

Hovenier, J. W., Multiple scattering of polarized light in planetary atmospheres, *Astron. Astrophys.*, *13*, 7–29, 1971.

Hovenier, J. W., and C. V. M. Van der Mee, Fundamental relationships relevant to the transfer of polarized light in a scattering atmosphere, *Astron. Astrophys.*, *128*, 1–16, 1983.

Kawabata, K., D. L. Coffeen, J. E. Hansen, W. A. Lane, M. Sato, and L. D. Travis, Cloud and haze properties from Pioneer Venus polarimetry, *J. Geophys. Res.*, *85*, 8129–8140, 1980.

Knibbe, W. J. J., J. F. De Haan, J. W. Hovenier, and L. D. Travis, A biwavelength analysis of Pioneer Venus polarization observations, *J. Geophys. Res.*, *102*, 10,945–10,957, 1997.

Knibbe, W. J. J., J. F. De Haan, J. W. Hovenier, and L. D. Travis, Analysis of temporal variations of the polarization of Venus observed by Pioneer Venus Orbiter, *J. Geophys. Res.*, *103*, 8557–8574, 1998.

Knollenberg, R. G., and D. M. Hunten, The microphysics of the clouds of Venus: Results of the Pioneer Venus particle size spectrometer experiment, *J. Geophys. Res.*, *85*, 8039–8058, 1980.

Mukai, S., and T. Mukai, Infrared properties of haze particles of Venus, *Icarus*, *48*, 482–487, 1981.

Na, C. Y., L. W. Esposito, and T. E. Skinner, International Ultraviolet Explorer observation of Venus SO^2 and SO, *J. Geophys. Res.*, *95*, 7485–7491, 1990.

Nagata, T., S. Sato, T. Mukai, and S. Mukai, Infrared polarization of Venus: Its periodic fluctuations and evidence for thin haze, *Icarus*, *57*, 125–134, 1984.

Pollack, J. B., E. F. Erickson, F. C. Witteborn, C. Chackerian, Jr., A. L. Summers, W. Van Camp, B. J. Baldwin, G. C. Augason, and L. J. Caroff, Aircraft observations of Venus' near-infrared reflection spectrum: Implications for cloud composition, *Icarus*, *23*, 8–26, 1974.

Pollack, J. B., E. F. Erickson, D. Goorvitch, B. J. Baldwin, D. W. Strecker, F. C. Witteborn, and G. C. Augason, A determination of the composition of the Venus clouds from aircraft observations in the near infrared, *J. Atmos. Sci.*, *32*, 1140–1150, 1975.

Pollack, J. B., D. W. Strecker, F. C. Witteborn, E. F. Erickson, and B. J. Baldwin, Properties of the clouds of Venus, as inferred from airborne observations of its near-infrared reflectivity spectrum, *Icarus*, *34*, 28–45, 1978.

Press, W. H., S. A. Teukolsky, W. T. Vetterling, and B. P. Flannery, *Numerical recipes: The art of scientific computing*, 2nd ed., Cambridge Univ. Press, New York, 1992.

Ragent, B. L., L. W. Esposito, M. G. Tomasko, M. Y. Marov, V. P. Shari, and V. N. Lebedev, Particulate matter in the Venus atmosphere, *Adv. Space Res.*, *5*, 85–115, 1985.

Russell, E. E., L. A. Watts, S. F. Pellicori, and D. L. Coffeen, Orbiter cloud photopolarimeter for the Pioneer Venus mission, *Proc. Soc. Photo. Opt. Instrum. Eng.*, *112*, 28–44, 1977.

Sato, M., L. D. Travis, and K. Kawabata, Photopolarimetry analysis of the Venus atmosphere in polar regions, *Icarus*, *124*, 569–585, 1996.

Sato, S., K. Kawara, Y. Kobayashi, H. Okuda, K. Noguchi, T. Mukai, and S. Mukai, Infrared polarization of Venus, *Icarus*, *43*, 288–292, 1980.

Travis, L. D., On the origin of ultraviolet contrasts on Venus, *J. Atmos. Sci.*, *32*, 1190–1200, 1975.

Travis, L. D., D. L. Coffeen, J. E. Hansen, K. Kawabata, A. A. Lacis, W. A. Lane, S. S. Limaye, and P. H. Stone, Orbiter cloud photopolarimeter investigation, *Science*, *203*, 781–785, 1979.

Van de Hulst, H. C., *Multiple Light Scattering: Tables, Formulas, and Applications*, Academic, San Diego, Calif., 1980.

C. J. Braak, J. F. de Haan, and J. W. Hovenier, Department of Physics and Astronomy, Free University, De Boelelaan 1081, NL-1081 HV Amsterdam, Netherlands. (rbraak@nat.vu.nl; johan@nat.vu.nl; hovenier@nat.vu.nl)

L. D. Travis, NASA Goddard Institute for Space Studies, 2880 Broadway, New York, NY 10025, USA. (ltravis@giss.nasa.gov)